Characterization of the mechanical properties of TPU fabricated by SLS in different printing orientations

Dror Raf[a], Itay Magen[a], Lee Jordan[a], Dana Solav[a,*]

[a] *Faculty of Mechanical Engineering, Technion Israel Institute of Technology, Haifa, 3200003, Israel*

Abstract

This study presents the mechanical characterization of a thermoplastic polyurethane (TPU) powder (FlexaBright™, Sinterit, Poland) fabricated by selective laser sintering (SLS). Despite its growing use in applications requiring elastomeric and rubber-like mechanical behavior, its characterization under finite tension and compression loads, as well as different print orientations, has not been thoroughly documented. To address this gap, we conducted uniaxial tension and compression tests on specimens printed in multiple orientations. The experiments included preconditioning cycles, measurement of force relaxation, and the estimation of equilibrium force using exponential decay fitting. Full-field strains were obtained using 3D digital image correlation (3D-DIC), and micro-CT scans were employed to accurately determine the specimens' cross-sectional areas. Elastic material parameters were estimated by fitting stress-strain data for the tension tests and by inverse finite element analysis of the compression data, for each print orientation. Although the Poisson's ratio remained similar across all tests, the results revealed clear anisotropy in the stiffness: horizontally printed specimens exhibited a Young's modulus that was 29% smaller in tension and 15% larger in compression compared to vertically printed specimens. These findings highlight the influence of print orientation on mechanical properties and provide essential material parameters for various engineering applications. Future research will explore the fitting of more complex anisotropic and viscoelastic models, as well as examine additional deformation regimes.

Keywords: 3D printing, additive manufacturing, elastic parameters, selective laser sintering, thermoplastic polyurethane, uniaxial tension and compression

---

1. Introduction

Additive manufacturing (AM) technologies offer new opportunities to fabricate structures with complex shapes and topologies that are difficult or impossible to achieve with conventional manufacturing methods, allowing unprecedented flexibility in design and fabrication across various applications and fields [1]. Among the various AM technologies, selective laser sintering (SLS) is an advanced AM technique that uses a high-power laser to fuse fine particles of powdered material into a desired three-dimensional (3D) solid structure. An SLS 3D printer typically

---

[*] Corresponding author

Email address: `danas@technion.ac.il` (Dana Solav)

spreads a thin layer of powder onto a build platform, which is then selectively sintered by the laser according to the cross-sections of the 3D computer-aided design (CAD) model and selected printing parameters. Once a layer is completed, the platform is lowered, and the next layer of powder is spread, repeating the process until the entire object is formed. SLS is particularly well-suited for producing complex geometries like porous and lattice structures, as it does not require the printing of support structures. The surrounding powder provides support for any overhanging parts during the printing process, and once the process is finished, the unsintered powder is removed and can be reused [2, 3, 4].

SLS is generally considered to produce parts with more isotropic mechanical properties compared to other AM methods, such as fused deposition modeling (FDM). However, several studies have reported noticeable levels of anisotropy in SLS printed components [5, 6]. Among the contributing factors, the orientation of the print has been identified as one of the most significant influences on anisotropic behavior [7].

Recently, a growing number of commercially available SLS systems have expanded the range of powdered materials they can process, moving beyond relatively stiff materials like Nylon or Polypropylene, to include softer, elastomeric materials such as thermoplastic polyurethane (TPU). TPU is widely used in biomedical devices, soft robotics, and smart polymer applications for its high elasticity and flexibility, making it ideal for creating parts that mimic the behavior of rubber-like materials [8].

FlexaBright™ (Sinterit, Poland) is a TPU powder designed for use with SLS printers, such as Lisa Pro (Sinterit, Poland), to fabricate flexible prototypes in a variety of applications. For example, Chick et al. [9] employed this material to produce complex knit-inspired geometries, and Capellini et al. [10] used it to generate clinically realistic 3D printed heart models for surgical planning. The mechanical properties reported by the manufacturer include tensile strength (10.3 MPa), elongation at break (318 %), and shore hardness (79 A). However, its elastic stiffness in the finite regime has not been reported by the manufacturer nor in the literature. Furthermore, the mechanical properties have not been reported for different printing orientations and different loading modes. Therefore, our objective is to characterize the mechanical properties of this material in tension and compression in different print orientations in the finite-strain regime and characterize these stress-strain relations by fitting them to appropriate constitutive material models.

2. Materials and Methods

This study investigates the mechanical properties of FlexaBright™ material (Sinterit, Warsaw, Poland) fabricated using Lisa Pro (Sinterit, Warsaw, Poland) SLS printer, under tension and compression large-deformation loadings. Uniaxial tension and compression tests were performed based on standard methods, as outlined in Section 2.1. Full-field displacement measurements were obtained using 3D digital image correlation (3D-DIC), as discussed in Section 2.3. Micro-CT scans were performed to obtain measurements of the cross-sectional area and internal microstructure, as described in Section 2.4. Finally, constitutive modeling and computation of material parameters from experimental data are detailed in Section 2.5.

2.1. Uniaxial tension and compression tests

The test specimens were modeled using Creo Parametric 8.0 (PTC, Inc., Boston, MA, USA) and processed with the Sinterit Studio Advance (Sinterit, Warsaw, Poland) printing slicer soft-

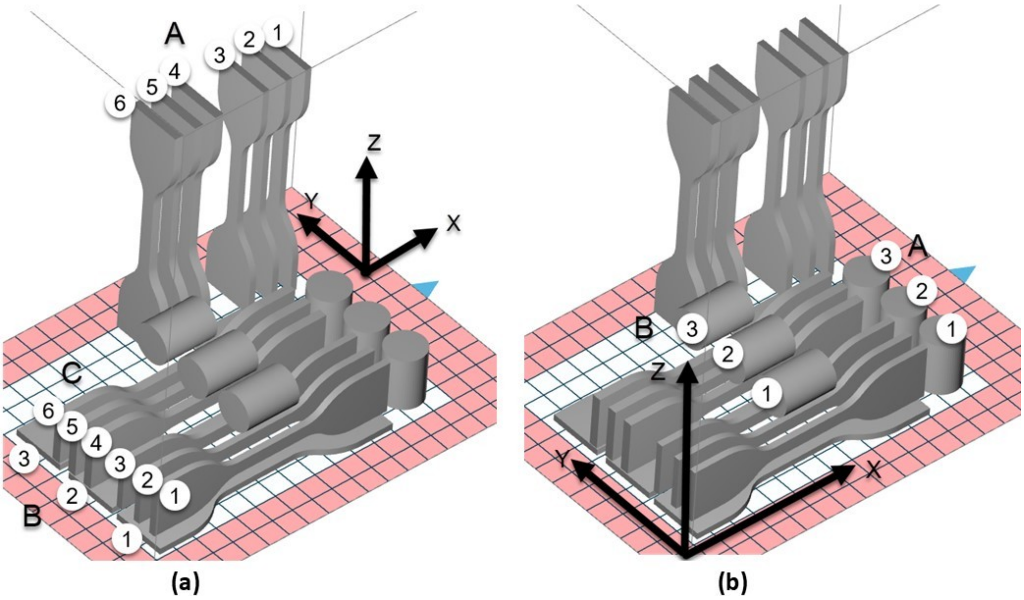

Figure 1: Print orientations and numbering of dumbbells (a) and cylinders (b) specimens. The layers of the printed specimen are built vertically along the Z direction. The X and Y directions are horizontal, while the Y direction is the direction in which the printer recoater is moving.

ware. The default parameters, including a layer height of 0.2 mm, were used to generate the g-code for the printer.

The geometry of the printed test specimens for uniaxial tension was based on the ASTM D412 Type-C standard [11]. The dumbbell specimen is suitable for tensile tests because it leads to homogeneous uniaxial stress and strain at the center of the specimen. To study the effect of printing orientation on mechanical properties, we printed specimens in three different orientations - one vertical and two horizontal, relative to the layer print directions. For convenience, we mark the specimens printed vertically as group A and the specimens printed horizontally as groups B and C. Multiple samples were printed for each group. In groups A and C, the specimens were printed with a thickness of 3 mm and 4 mm. Group B specimens were printed with a 3 mm thickness. The dumbbell specimens orientations and numbering are illustrated in Figure 1a.

The compression tests printed specimens geometry were based on the ISO 7743 standard [12]. For these tests, we printed cylindrical specimens with a diameter of 17.8 mm and a length of 25 mm in two printing orientations (horizontal and vertical). Three specimens were printed in each print orientation. We mark the cylinder models that were printed in the vertical direction as group A and the models that were printed in the horizontal direction as group B, as shown in Figure 1b.

The experiments were carried out using an eXpert 8000 horizontal planar biaxial testing system (ADMET, Inc., Norwood, MA, USA) with a 200 N load cell for the tension test and a 2000 N load cell for the compression test. The dumbbell specimens were mounted to the machine using eccentric roller grips, which self-tighten when the specimen thins under large elongation. The flat ends of the cylinders were glued to aluminum adapters that had a circular recess to which the compression platens attached. The experimental setup configurations for uniaxial tension and compression are shown in Figure 2.

The structural properties of elastomers typically change during the first several times the material is exposed to stress, resulting in a reduction in stiffness. This behavior is commonly known as Mullin's effect [13]. If an elastomer is loaded to a set strain value, followed by complete unloading to zero stress several times, the change in structural properties from cycle to cycle, as measured by the stress-strain curve, will diminish. When the stress-strain curve no longer changes significantly, the material may be considered to be stable for strain values smaller than that particular set strain maximum. For this reason, the tensile and compression test specimens were pre-conditioned by performing 10 cycles of engineering strain between 0% and approximately 20% at a constant displacement rate of 0.25 mm/s, after which the force-displacement curve has stabilized. After the pre-conditioning cyclic loading, we performed the uniaxial tension and compression tests with 7 and 5 equally spaced displacement steps, respectively. At each displacement step, the test was paused for 450 s, which was long enough to estimate the stable force. During this time, force measurements were taken every 1 s. As expected for a viscoelastic material subjected to constant strain, the measured force exhibits relaxation over time, and over a sufficiently long period, it asymptotically approaches a constant value [14]. Therefore, for each displacement step, the corresponding equilibrium force can be determined as the force predicted at infinite time, based on a chosen exponential decay model, as explained in Section 2.2. The dimensions of the samples were measured before and after pre-conditioning and before and after the tests to assess whether any plastic deformations occurred during the tests.

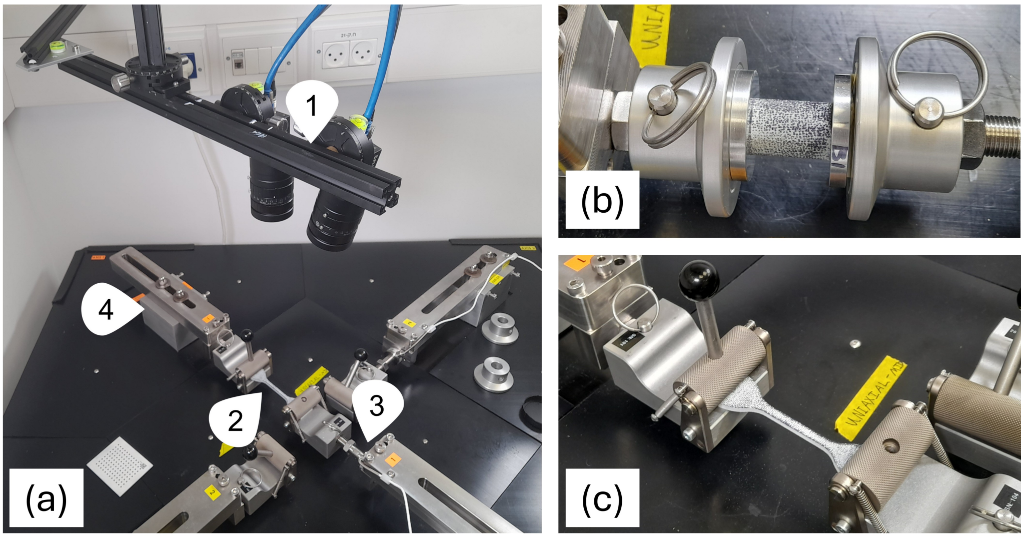

Figure 2: (a) Experimental setup for measuring the mechanical properties of FlexaBright™ material. (1) Two cameras in a stereo configuration. (2) test specimen (3) load cell. (4) horizontal planar biaxial testing system. (b) Compression cylinder specimen painted with random speckle pattern mounted at planer test machine gripers. (c) Tension dumbbell specimen painted with random speckle pattern, mounted with eccentric roller grips.

2.2. *Force data processing*

To obtain the equilibrium force from the force measurements that exhibit viscoelastic relxation, we used MATLAB's curve fitting tool (The Mathworks Inc., Natick, MA, USA), to fit the experimental force measurements to an exponential function with two terms:

$$F(t) = C_1 e^{-k_1 t} + C_2 e^{-k_2 t} + F_\infty \tag{1}$$

where $F(t)$ is the force value at time t, C_1 and C_2 are the amplitudes of the two exponential terms, k_1 and k_2 are the decay constants for each term, representing the rate at which the corresponding exponential terms decay, and F_∞ is the constant value that the force asymptotically approaches as $t \to \infty$, which is considered as the equilibrium force.

2.3. Full-field displacement and strain measurements

To obtain accurate strain measurement during the tests, we utilized 3D-DIC, a non-contact optical method that provides full-field measurements. These measurements allow for direct determination of both axial and transverse strains, allowing for the calculation of the Poisson's ratio, as well as the detection of local variations in strain.

The 3D-DIC test setup is shown in Figure 2a and exemplary full-field displacement results are shown in Figure 6. The 3D-DIC setup consists of two Blackfly BFS-U3-51SM-C cameras (FLIR LLC, Wilsonville, OR, USA) featuring a 5-megapixel monochrome Sony IMX264 sensor each equipped with a FUJINON HF25SA-1 lens with a focal length of 25 mm. The cameras were configured in a stereo arrangement and were synchronized to capture simultaneous images of the test specimens at each displacement step. The images were acquired and stored using QS-GRABBER software (MatchID Nv, Ghent, Belgium).

One camera was positioned perpendicular to the specimen's measured surface, and the second was placed at a stereo angle of 23 degrees. The standoff distance (SOD) between the cameras and the specimen was 350 mm. The specimens were manually painted with a random speckle pattern of average size 2.5 mm using black ink, as shown in Figure 2 (b) and (c). The intrinsic and extrinsic parameters of the cameras were calibrated using a calibration target measuring 9×12 cm with a grid of 9x12 5 mm diameter dots, using the MatchID stereo calibration software.

Next, the images were processed using the MatchID STEREO software to obtain full-field displacement maps within the selected region of interest (ROI). The following processing parameters were used:

- Subset size: 21 pixels
- Step size: 10 pixels
- Subset shape function: Affine
- Filtering: Gaussian kernel size 5

By spatially differentiating the displacement fields, the local strain fields were computed, using the following processing parameters:

- Strain window: 5
- Strain tensor: Logarithmic strain
- Interpolation: Bilinear quadrilateral

2.4. *Micro-CT scans*

We conducted micro-CT scans of the dumbbell and cylinder specimens using an N80 micro-CT scanner (NeoScan, Mechelen, Belgium). The scans were utilized to obtain an accurate measurement of the cross-sectional area of the specimens, since we suspected that their dimensions deviated from those specified in the CAD model. Obtaining an accurate measurement of the cross-sectional area is particularly important for computing the stress from the measured force.

This was accomplished by converting the DICOM image data into a MATLAB `.mat` file using the *dcmFolder2MATobject* function from the GIBBON toolbox version 3.5.0 [15]. The boundary contour of the cross-section was then extracted using the *imx* function, which identifies the contrast between the background and the specimen, as shown in Figure 3 and Figure 4 for dumbbells and cylinder specimens, respectively. The area of the specimen was calculated from the boundary contour using the *polyarea* function in MATLAB. For each specimen, three CT images were obtained, and the cross-sectional average area, A_0, was computed as the mean of the measurements from these images.

2.5. *Computation of material parameters from tension and compression test data*

The computation of material parameters from a set of experimental data involves choosing a material model with a set of material parameters and determining the set of parameters that minimizes the differences between the model's predictions and experimental results. To perform this optimization problem, we used the PolymerFEM MCalibration software [16], with the Nelder-Mead simplex optimization algorithm [17, 18].

The results of the uniaxial tension test in each (i^{th}) displacement step include the equilibrium force F_i predicted by fitting the exponential decay function in (1), and the logarithmic ("true") strains in the tensile direction, ε_i, and transverse direction, ε_i^t, obtained from the 3D-DIC measurements by averaging the strains across the region of interest. The uniaxial engineering stress is calculated by dividing F_i by the initial cross-sectional area, A_0, of the central region of the dumbbell specimen:

$$\sigma_i = F_i / A_0 \tag{2}$$

The compression tests do not yield homogeneous uniaxial conditions due to the adhesive bond between the cylinder and the plates. As a result, the force-displacement results cannot be used directly to obtain the stress-strain relationship. Instead, we use inverse finite element analysis (iFEA) to estimate the material parameters. This process involves constructing a simulation of the compression test using ANSYS Mechanical 2023 R2 (ANSYS, Inc., Canonsburg, PA, USA) and iteratively modifying the material parameters in an optimization loop within MCalibration software, until a convergence is reached between the experimental measurements and the simulation results. The FEA cylinder models were meshed using quadratic 20-node hexahedral elements (type SOLID186). Boundary conditions were prescribed to mimic the experiment. The flat ends of the cylinder were prescribed with displacements along the cylinder's axis, while fixed conditions were imposed in the other directions. To simplify the process, a single simulation was performed for each print orientation, based on the averaged force–displacement results from the experiments.

The objective function for minimizing the difference between the experimental values **e**, and the simulation-predicted values **p** was taken as the normalized mean absolute difference (NMAD) criterion, which is expressed as:

$$\text{NMAD}\ [\%] = 100 \cdot \frac{\langle |\mathbf{e} - \mathbf{p}| \rangle}{\max(\langle |\mathbf{e}| \rangle, \langle |\mathbf{p}| \rangle)} \tag{3}$$

Where ⟨·⟩ and |·| indicate mean and absolute values, respectively.

Selecting the most appropriate material model can be a challenging task, as it requires balancing between the model's accuracy and its simplicity. While a more complex model with numerous parameters may provide a better fit, it runs the risk of over-fitting and may lack physically meaningful parameters. In this work, we opted to fit a linear elastic model to each set of experiments, prioritizing model simplicity. Nevertheless, we openly share the experimental data to allow other researchers to attempt fitting other models to this data.

3. Results

3.1. Specimen dimensions

Table 1 and Table 2 present the dimensions of the dumbbell and cylindrical specimens, respectively. For the dumbbell specimens, each specimen has three different cross-sectional areas, based on: (1) the nominal CAD model; (2) measurements taken from the outer dimensions of the specimens using a caliper, and (3) computations derived from processing the micro-CT images, as detailed in Section 2.4. Similarly, the cross-sectional area of the cylindrical specimens is given based on capliper and micro-CT measurements, and their length is measured only using calipers. During the experiments, several specimens were damaged or failed unexpectedly. Therefore, only the results from intact specimens that demonstrated the expected behavior are included, maintaining their original numbering.

Notably, the dimensions of the 3D-printed specimens differ substantially from the dimensions of their CAD models. For the dumbbell specimens printed in the vertical direction (group A), the cross-section area is not rectangular but concavely rounded, as demonstrated in Figure 3.

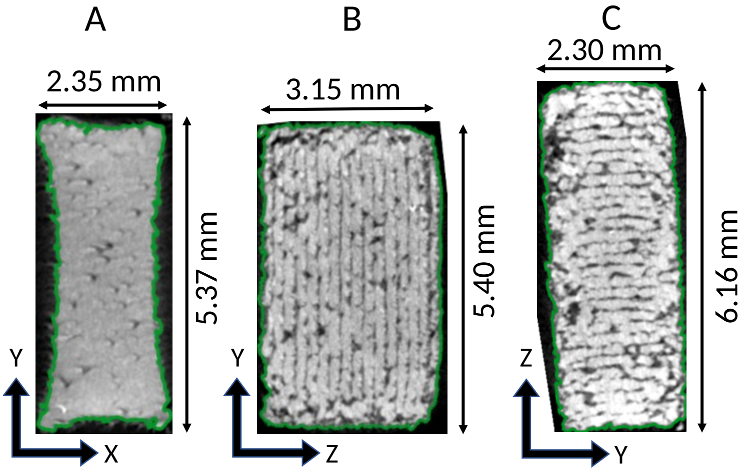

Figure 3: Micro-CT images of the dumbbell specimens 3D printed from FlexaBright™ TPU powder using SLS. The figure shows typical cross-section scans obtained for each print orientation (A, B, and C). The green boundary contour was used to calculate the cross-sectional area enclosed within it.

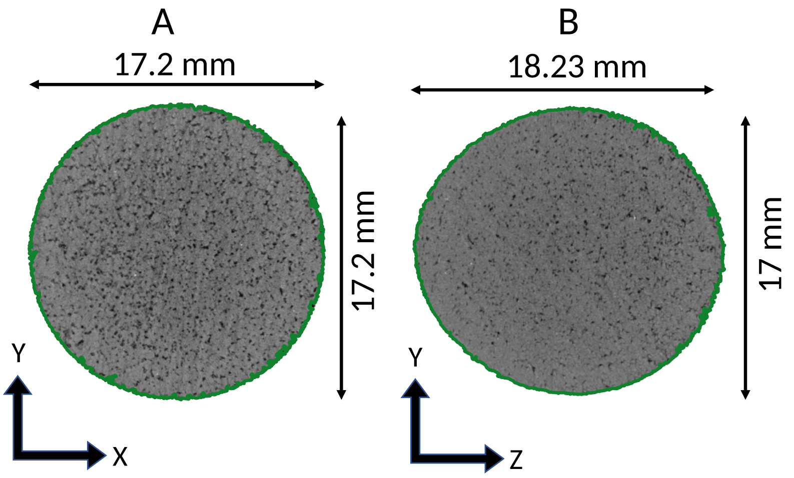

Figure 4: Micro-CT images of the cylinder specimens 3D printed from FlexaBright™ TPU powder using SLS. The figure shows typical cross-section scans obtained for each print orientation - A and B. The green boundary contour was used to calculate the cross-sectional area enclosed within it.

3.2. Exponential decay fitting

The relaxation behavior of the bulk material under constant strain was analyzed using the exponential decay model described in Section 2.2. The force at infinite time (F_∞) for each displacement step was determined by fitting the measured force relaxation data to (1). Figure 5 illustrates the adjustment process for a representative displacement step of the A2 dumbbell. The experimental force relaxation data points are shown alongside the fitted curve and the coefficient of determination (R^2), demonstrating excellent agreement between the model and the experimental results. The same fitting procedure was applied to all displacement steps of all specimens to obtain the values of F_∞, for which the elastic material parameters are fitted.

Table 1: Cross-sectional areas of dumbbell specimens as modeled and measured using caliper and micro-CT.

Group	**No.**	**Nominal area** [mm^2]	**Caliper measured area** [mm^2]	**Micro-CT images measured area** [mm^2]
A	**2**	18.0	12.3	9.4
	3	18.0	10.5	8.0
	4	24.0	17.9	14.0
	6	24.0	18.1	14.1
B	**1**	18.0	16.4	16.4
	2	18.0	16.9	16.8
	3	18.0	16.7	16.7
C	**1**	18.0	14.2	13.3
	2	18.0	14.2	13.1
	3	18.0	14.4	13.3
	4	24.0	20.4	19.0
	5	24.0	21.0	19.6

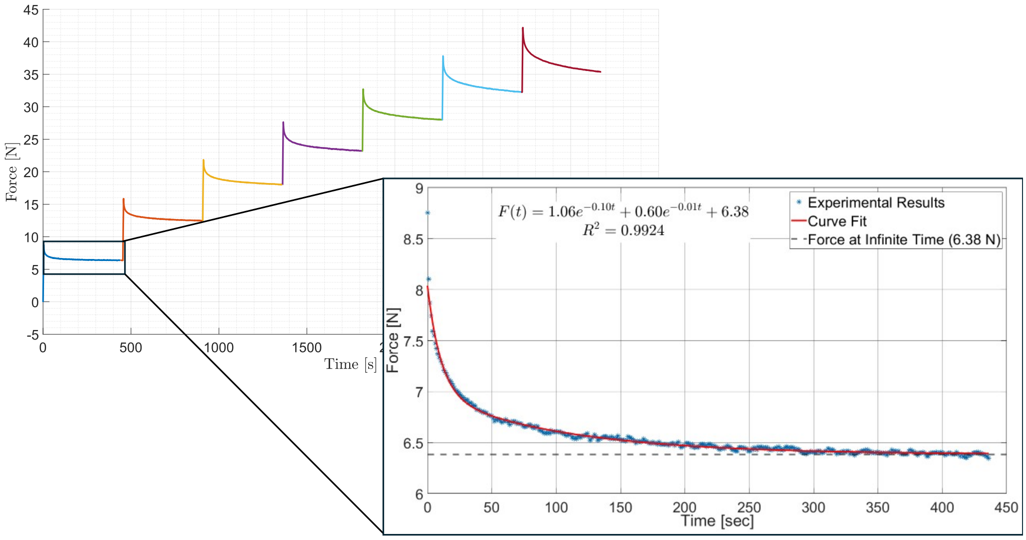

Figure 5: Force measurements of A2 dumbbell uniaxial tension test. The inset shows a zoomed-in view of the relaxation behavior observed during the first displacement step, and its fitting with the exponential decay function described in (1).

Table 2: lengths and cross-sectional areas of cylinder specimens as modeled and measured using caliper and micro-CT

Group	**No.**	**Caliper measured length** [mm]	**Caliper measured area** [mm^2]	**Micro-CT images measured area** [mm^2]
A	**1**	25.08	234.2	233.0
	2	25.16	234.0	231.5
	3	25.09	234.8	232.0
B	**1**	24.47	245.2	240.0
	3	24.44	243.0	238.0

3.3. Uniaxial tension and compression results

As detailed in Section 2.3, the strains in the uniaxial tension test were derived from the DIC measurements. Figure 6 illustrates the computed displacement and strain fields, showing that the dumbbell specimen exhibits homogeneous strain distribution, in contrast to the non-uniform strains observed in the cylindrical specimen.

The strain fields measured during the uniaxial tension tests were averaged for each displacement step. The results of tensile stress versus strain and transverse versus tensile strains, for dumbbell specimens from groups A, B, and C are presented in Figure 7 and Figure 8, respectively. The force-displacement results of the compression test on the cylindrical specimens from Groups A and B are shown in Figure 9.

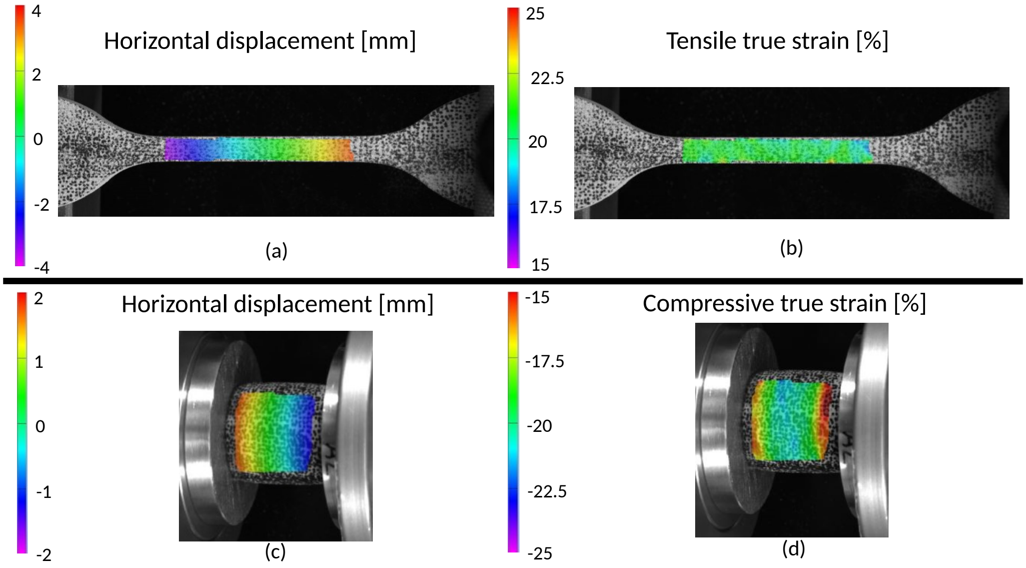

Figure 6: Displacement and strain maps obtained from DIC measurements. (a) horizontal displacement and (b) tensile true strain distribution in the ROI of the dumbbell specimen, showing a homogeneous strain field. (c) horizontal displacement and (d) compressive true strain distribution in the cylindrical specimen, showing non-homogeneous strains.

3.4. Fitting linear elastic material parameters to the experimental data

For the tension tests, the experimental data were fitted up to strain values of approximately 10%. In the compression tests, the fitting was performed for displacements up to 2 mm, which correspond to compressive strain values of approximately 10% relative to the specimen's initial length. Within this range, the stress-strain relationship exhibits approximately linear behavior. Therefore, we chose to fit the parameters according to a linear elastic constitutive model, for each print direction and loading mode.

The constitutive equation for a linear elastic material, also known as Hooke's law, is written as:

$$\varepsilon_{ij} = \frac{1+\nu}{E}\sigma_{ij} - \frac{\nu}{E}\sigma_{kk}\delta_{ij}, \tag{4}$$

where the Young's modulus E and the Poisson's ratio ν are the material parameters to be fitted, the indices i,j,k take the values 1, 2, and 3, and δ_{ij} is the Kronecker delta function defined by:

$$\delta_{ij} = \begin{cases} 1, & \text{if } i = j, \\ 0, & \text{if } i \neq j. \end{cases} \tag{5}$$

As explained in Section 2.5, since the tension experiments result in homogeneous and uniaxial loading conditions, the parameters are fitted directly to the stress-strain curves computed from the experiment. In contrast, the compression tests yield inhomogeneous loadings, and the force-displacement results are used to fit the material parameters in an iFEA procedure.

Figure 7 and Figure 8 present the parameter fitting for the results of the tensile tests of specimens from group A and groups B and C according to tensile stress-strain and the transverse-tensile strain relationships, respectively. Figure 9 presents the FEA-based predictions against the experimental measurements for the compression test of groups A and B. These results demonstrate the adequacy of the linear approximation within the specified strain range. The fitted parameters and the NAMD fitness results for all print orientations are summarized in Table 3.

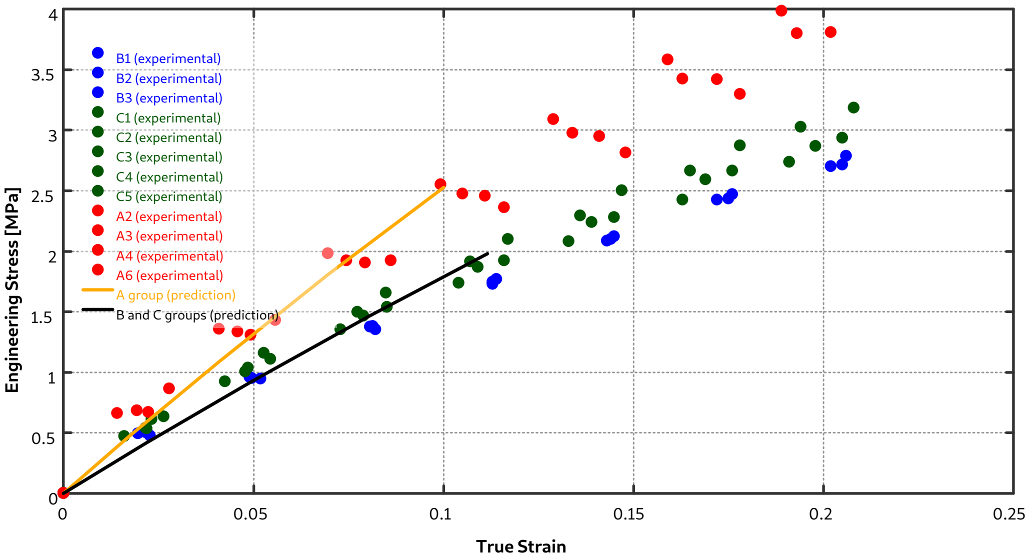

Figure 7: Uniaxial tension response of the dumbbell specimens. The plot shows tensile engineering stress versus true tensile strain for different specimen groups varying by their print orientation. The yellow and black solid lines are linear elastic model predictions, for group A and groups B and C, respectively, fitted up to strain values of approximately 10%.

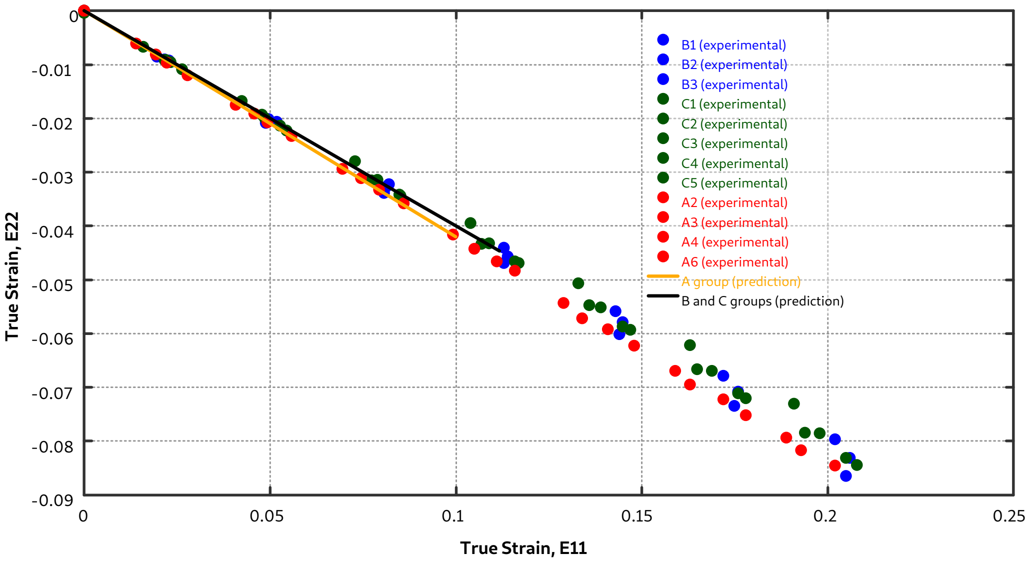

Figure 8: Transverse strain (E22) versus true tensile strain (E11) obtained from uniaxial tension tests for different specimen groups varying by their print orientation. The yellow and black solid lines are linear elastic model predictions, for group A and groups B and C, respectively, fitted up to strain values of approximately 10%.

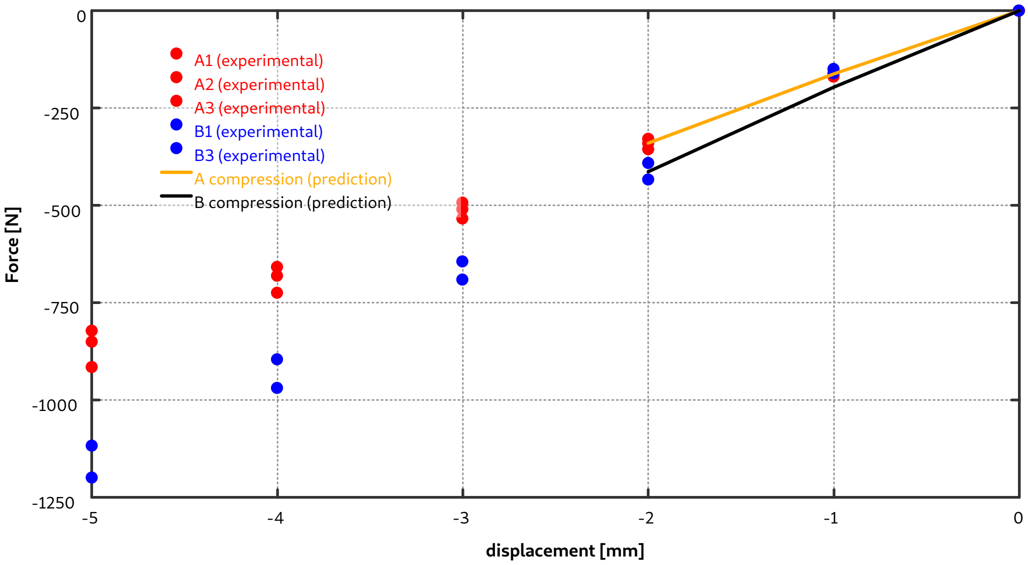

Figure 9: Force-displacement results for the compression tests of the cylindrical specimens. Specimens in group A (printed vertically) and B (printed horizontally) are plotted in red and blue, respectively. The yellow and black solid lines are linear elastic model predictions, for group A and group B, respectively, fitted up to a displacement of 2 mm.

Table 3: Elastic modulus (E), Poisson's ratio (ν), and NMAD values for different deformation modes and print orientations

Print orientation	Test deformation	E [MPa]	ν [-]	NMAD [%]
Vertical	Tension	27.5	0.42	16.4
Horizontal	Tension	19.4	0.40	16.9
Vertical	Compression	15.0	0.42	0.95
Horizontal	Compression	17.3	0.40	6.66

4. Discussion and Conclusions

This study characterized the mechanical response of the TPU material, FlexaBright™, additively manufactured using SLS, under tension and compression loadings, in multiple print orientations. This was important since signing and fabricating parts using SLS with this material often requires detailed knowledge of its mechanical properties, which was absent in the literature. The first step of this study involved fabricating dumbbell and cylindrical test specimens in multiple printing orientations. Next, we conducted tension and compression experiments to determine their elastic response. Finally, we characterized their elastic properties by fitting the data to a linear elastic model.

The measured dimensions of the specimens differed substantially from the nominal dimensions of the 3D models. A dimensional reduction is observed in the X and Y directions, whereas an expansion occurs along the Z direction. This discrepancy is likely due to the specific conditions and parameters of the 3D printing process. As previously reported for other SLS printers, temperature gradients in the build chamber and differential shrinkage between adjacent layers contribute to dimensional deviations [19, 20, 21].

Notably, measurements obtained from micro-CT scans indicated that the cross-sectional geometry of some specimens, particularly those printed vertically (group A), deviated from the expected rectangular shape and presented substantially smaller cross-sectional areas than those specified in the 3D model. These artifacts can be mitigated by optimizing the printing parameters and the implementation of the SLS technology [22]. However, in the context of this study, which aimed to characterize the printed material's mechanical response, we did not attempt to manufacture specimens with more accurate dimensions. Instead, we accurately measured cross-sectional areas using micro-CT and 3D strains using DIC to obtain accurate data for fitting material parameters.

In the uniaxial tension tests, the material exhibited approximately linear stress-strain response within the tested deformation range, supporting the choice of fitting a linear elastic model for this range. The relatively large values of the NMAD fitness (16.9 and 16.4 for the vertical and horizontal orientation groups, respectively) are owed partially to the variability between the specimens and partially to the nonlinear response of the materials. Notable differences were observed between group A specimens, which were printed vertically along the layers' Z-axis, and groups B and C, which were printed horizontally, in the X-Y and X-Z planes, respectively. The fitted Young's moduli present a 29% smaller stiffness for groups B+C relative to group A. These variations are attributed to the inherent anisotropy of the SLS printing process. This finding aligns with previous works that reported orientation-dependent tensile response for polyamide 12 (PA12) parts printed by SLS [23, 24, 25]. Xu et al. (2020) [26] reported that the Young's moduli of SLS-printed TPU vary with print orientation, with a higher stiffness observed in horizontally printed specimens (19 MPa compared to 29 MPa), contrary to our findings. In addition to differences in experimental conditions, such as the SLS machine, printing parameters, and type of TPU powder, the tensile stress was calculated using the nominal cross-sectional area. In contrast, in our work, the actual cross-sectional areas of the fabricated specimens were measured. Since we measured substantially smaller cross-sectional areas than those specified in the 3D model for group A (vertical), computing the stress using the measured area rather than the nominal one, substantially impacted the Young's moduli. As illustrated in Figure 3 and described in previous studies on PA12 [25, 27], the microstructure of the printed layers, and particularly the porosity level and morphology, varies with orientation. This phenomenon is likely the main contributor to the observed discrepancies in the mechanical response. Despite these differences in stiffness, the Poisson ratio was found to be similar in all cases, ranging between 0.40 – 0.42.

In the compression tests, group A (vertical) also displayed distinct behavior relative to group B (horizontal). However, in contrast to the behavior in tension, the stiffness of group A was smaller than in group B. Despite these differences, all groups maintained an approximately linear relationship within the tested range, as indicated by the small NMAD values resulting from fitting a linear elastic model. To the best of our knowledge, no previous studies have been published on how compressive properties are influenced by print orientation.

Future work may extend the mechanical characterization of FlexaBright™ and other TPU powders by analyzing their time-dependent behavior to fit viscoelastic models [28], by fitting the orientation-dependent response to anisotropic constitutive models, or by fitting experimental data over a larger deformation range to nonlinear constitutive models. Furthermore, the experimental tests can be extended to include additional deformation modes such as shear and biaxial loadings

[29]. Moreover, the investigation of the microstructure contribution to the anisotropic responses can be performed by analyzing the porosity levels and the pore morphology [30]. Investigating the effect of various printing parameters on these measured values can further enhance our understanding of the mechanical properties of parts manufactured from TPU powder using SLS [31].

References

[1] K. V. Wong, A. Hernandez, A Review of Additive Manufacturing, ISRN Mechanical Engineering 2012 (2012) 1–10. doi:10.5402/2012/208760.

[2] S. F. S. Shirazi, S. Gharehkhani, M. Mehrali, H. Yarmand, H. S. C. Metselaar, N. Adib Kadri, N. A. A. Osman, A review on powder-based additive manufacturing for tissue engineering: selective laser sintering and inkjet 3D printing, Science and Technology of Advanced Materials 16 (2015) 033502. URL: http://www.tandfonline.com/doi/full/10.1088/1468-6996/16/3/033502. doi:10.1088/1468-6996/16/3/033502.

[3] A. Mazzoli, Selective laser sintering in biomedical engineering, Medical & Biological Engineering & Computing 51 (2013) 245–256. URL: http://link.springer.com/10.1007/s11517-012-1001-x. doi:10.1007/s11517-012-1001-x.

[4] I. Gibson, D. Rosen, B. Stucker, M. Khorasani, Additive Manufacturing Technologies, Springer International Publishing, Cham, 2021. URL: https://link.springer.com/10.1007/978-3-030-56127-7. doi:10.1007/978-3-030-56127-7.

[5] J. R. C. Dizon, A. H. Espera Jr, Q. Chen, R. C. Advincula, Mechanical characterization of 3D-printed polymers, Additive manufacturing 20 (2018) 44–67. Publisher: Elsevier.

[6] W. Cooke, R. Anne Tomlinson, R. Burguete, D. Johns, G. Vanard, Anisotropy, homogeneity and ageing in an SLS polymer, Rapid Prototyping Journal 17 (2011) 269–279. URL: https://www.emerald.com/insight/content/doi/10.1108/13552541111138397/full/html. doi:10.1108/13552541111138397.

[7] N. Zohdi, R. C. Yang, Material Anisotropy in Additively Manufactured Polymers and Polymer Composites: A Review, Polymers 13 (2021) 3368. URL: https://www.mdpi.com/2073-4360/13/19/3368. doi:10.3390/polym13193368.

[8] S. M. Desai, R. Y. Sonawane, A. P. More, Thermoplastic polyurethane for three-dimensional printing applications: A review, Polymers for Advanced Technologies 34 (2023) 2061–2082. URL: https://onlinelibrary.wiley.com/doi/10.1002/pat.6041. doi:10.1002/pat.6041.

[9] M. Chick, C. Ho, J. Au, S. Wong, J. Yip, Combination of 3D printing and knitting: the loop stitch design and its effects on tensile strength and elongation at break, International Journal of Fashion Design, Technology and Education (2024) 1–10. URL: https://www.tandfonline.com/doi/full/10.1080/17543266.2024.2375652. doi:10.1080/17543266.2024.2375652.

[10] K. Capellini, L. Ait-Ali, V. Pak, M. Cantinotti, M. Murzi, E. Vignali, B. M. Fanni, A. Clemente, S. Celi, E. Gasparotti, Three-dimensional printed models as an effective tool for the management of complex congenital heart disease, Frontiers in Bioengineering and Biotechnology 12 (2024) 1369514. URL: https://www.frontiersin.org/articles/10.3389/fbioe.2024.1369514/full. doi:10.3389/fbioe.2024.1369514.

[11] D. ASTM, Standard test methods for vulcanized rubber and thermoplastic elastomers-tension, ASTM D412-16 (2006).

[12] I. O. f. Standardization, ISO 7743: 2011: Rubber, Vulcanized Or Thermoplastic. Determination of Compression Stress-strain Properties, ISO, 2011.

[13] L. Mullins, Softening of rubber by deformation, Rubber chemistry and technology 42 (1969) 339–362.

[14] W. Fliige, Viscoelasticity, Blaisdell Publ. Comp., London (1967) 1069–1084. Publisher: Springer.

[15] K. M. Moerman, GIBBON: the geometry and image-based bioengineering add-on, Journal of Open Source Software 3 (2018) 506.

[16] J. Bergstrom, PolymerFEM LLC (2023). MCalibration version: 6.6.0. Dover, MA., 2023. URL: https://polymerfem.com.

[17] X.-S. Yang, Nature-inspired optimization algorithms, Academic Press, 2020.

[18] R. K. Arora, Optimization: algorithms and applications, CRC press, 2015.

[19] M. Fahad, N. Hopkinson, Evaluation and comparison of geometrical accuracy of parts produced by sintering-based additive manufacturing processes, The International Journal of Advanced Manufacturing Technology 88 (2017) 3389–3394. Publisher: Springer.

[20] H.-J. Yang, P.-J. Hwang, S.-H. Lee, A study on shrinkage compensation of the SLS process by using the Taguchi method, International Journal of Machine Tools and Manufacture 42 (2002) 1203–

1212. URL: https://linkinghub.elsevier.com/retrieve/pii/S0890695502000706. doi:10.1016/S0890-6955(02)00070-6.

[21] P. Mantada, R. Mendricky, J. Safka, PARAMETERS INFLUENCING THE PRECISION OF VARIOUS 3D PRINTING TECHNOLOGIES, MM Science Journal 2017 (2017) 2004–2012. URL: http://www.mmscience.eu/december-2017.html#201776. doi:10.17973/MMSJ.2017_12_201776.

[22] S. Yuan, F. Shen, J. Bai, C. K. Chua, J. Wei, K. Zhou, 3D soft auxetic lattice structures fabricated by selective laser sintering: TPU powder evaluation and process optimization, Materials and Design 120 (2017) 317–327. URL: http://dx.doi.org/10.1016/j.matdes.2017.01.098. doi:10.1016/j.matdes.2017.01.098, publisher: Elsevier Ltd.

[23] F. Calignano, F. Giuffrida, M. Galati, Effect of the build orientation on the mechanical performance of polymeric parts produced by multi jet fusion and selective laser sintering, Journal of Manufacturing Processes 65 (2021) 271–282. URL: https://linkinghub.elsevier.com/retrieve/pii/S1526612521001845. doi:10.1016/j.jmapro.2021.03.018.

[24] I. Jevtić, Z. Golubović, G. Mladenović, F. Berto, A. Sedmak, A. Milovanović, M. Milošević, Printing orientation influence on tensile strength of PA12 specimens obtained by SLS, Journal of Mechanical Science and Technology 37 (2023) 5549–5554. URL: https://link.springer.com/10.1007/s12206-023-2306-4. doi:10.1007/s12206-023-2306-4.

[25] M. K. Razaviye, R. A. Tafti, M. Khajehmohammadi, An investigation on mechanical properties of PA12 parts produced by a SLS 3D printer: An experimental approach, CIRP Journal of Manufacturing Science and Technology 38 (2022) 760–768. URL: https://linkinghub.elsevier.com/retrieve/pii/S1755581722001249. doi:10.1016/j.cirpj.2022.06.016.

[26] T. Xu, W. Shen, X. Lin, Y. M. Xie, Mechanical Properties of Additively Manufactured Thermoplastic Polyurethane (TPU) Material Affected by Various Processing Parameters, Polymers 12 (2020) 3010. URL: https://www.mdpi.com/2073-4360/12/12/3010. doi:10.3390/polym12123010, number: 12 Publisher: Multidisciplinary Digital Publishing Institute.

[27] N. Majca-Nowak, E. Kluska, P. Gruda, Comparative Analysis of Macro- and Microstructure of Printed Elements in the FDM, SLS and MJ Technologies, Transactions on Aerospace Research 2019 (2019) 66–80. URL: https://www.sciendo.com/article/10.2478/tar-2019-0024. doi:10.2478/tar-2019-0024.

[28] M. Kadkhodaei, M. Pawlikowski, R. Drobnicki, J. Domański, An experimental and theoretical investigation on the hyper-viscoelasticity of polyamide 12 produced by selective laser sintering, PLOS ONE 19 (2024) e0304823. URL: https://dx.plos.org/10.1371/journal.pone.0304823. doi:10.1371/journal.pone.0304823.

[29] M. Sasso, G. Palmieri, G. Chiappini, D. Amodio, Characterization of hyperelastic rubber-like materials by biaxial and uniaxial stretching tests based on optical methods, Polymer Testing 27 (2008) 995–1004. URL: https://linkinghub.elsevier.com/retrieve/pii/S0142941808001529. doi:10.1016/j.polymertesting.2008.09.001.

[30] G. Flodberg, H. Pettersson, L. Yang, Pore analysis and mechanical performance of selective laser sintered objects, Additive Manufacturing 24 (2018) 307–315. URL: https://linkinghub.elsevier.com/retrieve/pii/S2214860418306699. doi:10.1016/j.addma.2018.10.001.

[31] V. M. Bruère, A. Lion, J. Holtmannspötter, M. Johlitz, The influence of printing parameters on the mechanical properties of 3D printed TPU-based elastomers, Progress in Additive Manufacturing 8 (2023) 693–701. URL: https://link.springer.com/10.1007/s40964-023-00418-7. doi:10.1007/s40964-023-00418-7.